Atmos. Meas. Tech. Discuss., 5, 1717–1761, 2012
www.atmos-meas-tech-discuss.net/5/1717/2012/
doi:10.5194/amtd-5-1717-2012

Atmospheric Measurement Techniques Discussions

Observations of tropical rain with a polarimetric X-band radar: first results from the CHUVA campaign

M. Schneebeli[1,2], J. Sakuragi[1], T. Biscaro[1], C. F. Angelis[1], I. Carvalho da Costa[1], C. Morales[3], L. Baldini[4], and L. A. T. Machado[1]

[1]Instituto Nacional de Pesquisas Espaciais (INPE), Centro de Previsão de Tempo e Estudos Climáticos (CPTEC), Cachoeira Paulista, Brazil
[2]École Polytechnique Fédérale de Lausanne (EPFL), School of Architecture, Civil and Environmental Engineering (ENAC), Lausanne, Switzerland
[3]Instituto de Astronomia, Geofisica e Ciéncias Atmosféricas, Universidade de São Paulo, São Paulo, Brazil
[4]Instituto di Scienze dell'Atmosfera e del Clima (CNR), Rome, Italy

Received: 23 January 2012 – Accepted: 10 February 2012 – Published: 17 February 2012

Correspondence to: M. Schneebeli (marc.schneebeli@epfl.ch)

Published by Copernicus Publications on behalf of the European Geosciences Union.

Abstract

A polarimetric X-band radar has been deployed during one month (April 2011) for a field campaign in Fortaleza, Brazil, together with additional sensors like a Ka-band vertically pointing frequency modulated continuous wave (FMCW) radar and three laser disdrometers. The disdrometers as well as the FMCW radar are capable of measuring the rain drop size distributions (DSDs), hence making it possible to forward-model theoretical polarimetric X-band radar observables at the point where the instruments are located. This set-up allows to thoroughly test the accuracy of the X-band radar measurements as well as the algorithms that are used to correct the radar data for radome and rain attenuation. In the first campaign in Fortaleza it was found that radome attenuation dominantly affects the measurements. With an algorithm that is based on the self-consistency of the polarimetric observables, the radome induced reflectivity offset was estimated. Offset corrected measurements were then further corrected for rain attenuation with two different schemes. The performance of the post-processing steps is being analyzed by comparing the data with disdrometer-inferred polarimetric variables that were measured in a distance of 20 km to the radar.

1 Introduction

The usage of conventional single polarization X-band weather radars was limited to target applications on small rural or urban basins, and also serving as a gap filler of conventional weather radar networks (e.g. Delrieu et al., 1999). When dual-polarization X-band radars became available in the last decade (Zrnic and Ryzhkov, 1999), that had the capability of correcting rain attenuation in a reliable manner (Testud et al., 2000; Anagnostou et al., 2004; Gorgucci et al., 2006), these instruments became a popular tool for various applications related to the measurement of precipitation at small to medium scales (≈1–50 km), which culminated in the proposal of networking operation with the potential to cover wide areas (like e.g. the CASA project; McLaughlin et al., 2009; Wang and Chandrasekar, 2010).

AMTD
5, 1717–1761, 2012

The fact that X-band radars are small and therefore easy to deploy makes it attractive for using them in field campaigns, hence numerous field studies made use of X-band radar measurements up to now: the HMT campaign (Matrosov, 2010) as well as the campaign described in Schneebeli et al. (2010) were focusing on measurements of snowfall, while others aimed at the understanding of the microphysics of precipitation (Berne et al., 2005; Anagnostou et al., 2006).

In April 2011, the first field campaign of the CHUVA project took place in Fortaleza, on the northeastern coast of Brazil. CHUVA (being the Portuguese word for rain; the acronym stands for "**C**loud processes of t**H**e main precipitation systems in Brazil: A contrib**U**tion to cloud resol**V**ing modeling and to the GPM (Glob**A**l Precipitation Measurement)") aims at resolving microphysical processes that occur in tropical clouds in order to better understand formation of severe precipitation. The set-up of remote sensors consisted of an X-band polarimetric weather radar (see e.g. Bechini et al., 2010), a 24 GHz vertically pointing Micro Rain Radar (MRR; Peters et al., 2002), a Raymetrics Raman lidar, and a Radiometrics passive microwave temperature and humidity profiler (Ware et al., 2003) and was complemented by a wealth of ground-based (disdrometers, rain gauges, anemometric tower) and air-borne (triangle of radiosondes launched every six hours) in-situ sensors. With this sensor assembly deployed in the tropics, a detailed assessment of processes governing the formation of clouds and precipitation becomes feasible. The focus of the first campaign in Fortaleza was put on the detection of warm clouds, i.e. clouds that do not exceed the melting layer and therefore form precipitation without the influence of the ice phase. Rain events originating from warm clouds can be very hazardous, but detection with traditional satellite-based precipitation estimation schemes is difficult due to the lack of the ice phase of these clouds and therefore remains an unresolved problem. It is expected that the results from the Fortaleza campaign will improve the understanding of warm rain events and eventually lead to better rain estimates over land. Following the campaign in Fortaleza, the whole sensor assembly moved to Belém. The focus of the Belém campaign, which took place in June 2011, was put on tropical squall-lines and their associated processes that form

AMTD
5, 1717–1761, 2012

intense tropical precipitation. In order to make the radar data useful for any quantitative analysis and for using it in microphysical studies, several post-processing steps are necessary, such as radome and rain attenuation correction, differential reflectivity correction, estimation of the specific differential phase and hydrometeor identification. Several algorithms capable of tackling these tasks were implemented (ZPHI algorithm for attenuation correction (Testud et al., 2000), for attenuation correction, the algorithm from Hubbert and Bringi (1995) for the estimation of the accumulated and specific differential propagation phase shift Φ_{dp} and K_{dp}, respectively, as well as the extended Kalman filter (EKF) algorithm from Schneebeli and Berne (2012) for radome and rain attenuation correction and estimation of K_{dp} and Φ_{dp}) and tested on the first available data sets from the Fortaleza campaign. Rain drop size distributions (DSD's) provided by the disdrometers are being used to forward-model the radar polarimetric variables by employing the T-matrix method (Mishchenko and Travis, 1998). The results of this modeling approach are further being used for the correct adaptation of existing attenuation correction schemes to the conditions at the site in Brazil. The details of these algorithms will be described and it will also be shown how they perform by comparing radar measurements with the polarimetric moments inferred from DSD measurements of a Parsivel disdrometer located in a distance of 20 km to the radar.

The article is organized as follows: in Sect. 2, specifications of the radar, the disdrometer and the measurements associated with these instruments are described. In Sect. 3, it is shown how polarimetric moments are calculated from the disdrometer measurements. These simulations are then used in the Sects. 4 and 5, where the attenuation correction with the ZPHI algorithm is described and the EKF method is introduced, respectively. Methods for correcting Z_{dr} are provided in Sect. 6. Finally, the results for the radome and rain attenuation correction and the data processing with the EKF and ZPHI methods are given in Sect. 7 and conclusions are drawn in Sect. 8.

AMTD
5, 1717–1761, 2012

2 Campaign set-up and instruments

2.1 The campaign in Fortaleza

Fortaleza (3.43° S, 38.30° W) is located at the northern coast of Brazil and counts around 2.5 million inhabitants. The radar was installed on a 5 m high temporary tower that was erected in a neighboring suburb called Eusebio. Within the city of Fortaleza, a measurement site was established that was equipped with a the Parsivel disdrometer, the MRR and the additional ground-based instruments. The distance between the radar and the measurement site in the city was 20 km. On average, Fortaleza receives 350 mm of rain during April and the daily mean temperature is 27 °C.

2.2 Radar specifications and scanning strategy

A mobile 9.345 GHz dual-polarization radar, manufactured by Gematronik, Germany, was employed. Its main characteristics are summarized in Table 1.

The radar provides the standard polarimetric observables: reflectivity in horizontal polarization (Z_h [dBZ]), differential reflectivity (Z_{dr} [dB]), differential phase shift (Ψ_{dp} [°]), specific differential phase shift (K_{dp} [° km^{-1}]), copolar correlation coefficient (ρ_{hv} [–]) as well as the Doppler variables velocity (v_D [m s^{-1}]) and velocity spectrum width (σ_{v_D} [m s^{-1}]). An example of one range-height indicator (RHI) scan of the radar's polarimetric variables is shown in Fig. 1.

The strategy for the Fortaleza campaign includes a Z_{dr} calibration scan (89° elevation with high speed; 89° instead of 90° elevation had to be chosen due to a limitation in the radar control software), two RHI scans with high angular resolution (0.5°) and high sampling frequency (150 independent samples per ray). One RHI was directed towards the heavily equipped ground site located in 20 km distance to the radar where also the Parsivel disdrometer is located that will later be used for evaluating the radar's polarimetric moments. The other RHI pointed toward the sea in the direction where the main weather systems are expected to enter the continent. The volume was scanned

AMTD
5, 1717–1761, 2012

with 13 elevations from 1.8° to 21.4° with a spacing of 1.1° between the lowermost elevations and a spacing of 2.8° between the uppermost elevations. The lowest elevation was set to 1.8° since there was almost complete signal blocking below this angle. A fixed clutter filter width of 1.44 m s^{-1} was used and in addition, the strong signal blocking at low elevations acted like a clutter fence, hence the clutter contamination at higher elevations was low. One complete scanning cycle consisting of the mentioned two RHI scans, the volume scan and the Z_{dr} calibration was completed within 6 min.

2.3 Disdrometers

The Parsivel laser disdrometers are capable of measuring the DSD of precipitation, i.e. the particle density per size class. A horizontal laser beam provides a sampling area of 54 cm^2. When a particle crosses the laser beam, the intensity loss of the received laser signal as well as the time the particle remains in the beam are used to estimate the drop's equivolumetric diameter D and its fall velocity v. The estimated sizes and fall speeds are stored in 32 × 32 matrix corresponding to 32 non-equidistant diameter classes (from 0 to 25 mm) and 32 non-equidistant velocity classes (from 0 to 22.4 m s^{-1}). From this raw diameter-velocity spectrum, not only the rain rate R can be calculated but also the DSD $N(D)$, i.e. the drop concentration per volume and per diameter size class. Details on this procedure can be found in Battaglia et al. (2010) and Jaffrain and Berne (2011).

3 T-Matrix modeling

The polarimetric variables K_{dp} [° km^{-1}], $Z_{h,v}$ [mm^6 m^{-3}], the differential phase shift on backscatter δ_{hv} [°] as well as the specific one-way attenuation $A_{h,v}$ [dB km^{-1}] were calculated from the DSDs ($N(D)$) provided by the Parsivel disdrometer with following

AMTD
5, 1717–1761, 2012

formulae (e.g. Bringi and Chandrasekar, 2001):

$$K_{\mathrm{dp}} = \frac{180\lambda}{\pi} \int_{D_{\min}}^{D_{\max}} \mathrm{Re}[f_{\mathrm{hh}}(D) - f_{\mathrm{vv}}(D)] N(D) dD \quad (1)$$

$$Z_{\mathrm{h,v}} = \frac{4\lambda^4}{\pi^4} \left| \frac{N_{\mathrm{r}}^2 + 2}{N_{\mathrm{r}}^2 - 1} \right| \int_{D_{\min}}^{D_{\max}} \left| s_{\mathrm{hh,vv}}(D) \right|^2 N(D) dD \quad (2)$$

$$\delta_{\mathrm{hv}} = \frac{180}{\pi} \arg \left[\int_{D_{\min}}^{D_{\max}} s_{\mathrm{hh}} s_{\mathrm{vv}}^* N(D) dD \right] \quad (3)$$

$$A_{\mathrm{h,v}} = 8.68\lambda \int_{D_{\min}}^{D_{\max}} \mathrm{Im}\left[f_{\mathrm{hh,vv}} \right] N(D) dD \quad (4)$$

where λ is the wavelength [mm], N_{r} the refractive index of water (dimensionless), $f_{\mathrm{hh,vv}}$ the forward- and $s_{\mathrm{hh,vv}}$ the backward-scattering amplitude in [m] at horizontal (hh) or vertical (vv) polarization. Re and Im denote the real and imaginary part, respectively, arg the argument and * the complex conjugate.

The scattering amplitudes can be calculated with the method known as T-matrix (Barber and Yeh, 1976) and the freely available Fortran implementation of Mishchenko and Travis (1998) was used for computation. The shape of the raindrops was approximated by an oblate spheroid. The axial ratio of the spheroid, being a function of the equivolumetric sphere diameter, were calculated with the models of Andsager et al. (1999), Brandes et al. (2002) and Thurai and Bringi (2005). The refractive index of water was calculated with the model of Meissner and Wentz (2004). Calculations were made at a frequency of 9.345 GHz, at a temperature of 300 K and with 23 diameter size classes

AMTD
5, 1717–1761, 2012

ranging from $D_{min} = 0.062$ mm to $D_{max} = 7.5$ mm. The size classes were predefined by the Parsivel instrument. The two smallest size classes (0.062 mm and 0.187 mm) are always empty due to signal-to-noise limitations for these small diameters, hence the lowermost detectable diameter is 0.312 mm.

From the variables defined in Eqs. (1) and (3), Φ_{dp} and Ψ_{dp} can be estimated as follows:

$$\Phi_{dp} = 2 \int_0^{r_{max}} K_{dp}(r)\, dr \tag{5}$$

$$\Psi_{dp} = \Phi_{dp} + \delta_{hv} \tag{6}$$

Relations between the rain rate R and Z_h or K_{dp} are of particular interest for any application focusing on quantitative precipitation estimation (QPE). Since the body of literature on such relations for X-band frequencies in tropical regions is small, we have plotted our modeling results in Fig. 2. The corresponding power law relations that were found by linearly fitting the logarithm of R with the logarithm of the modeled K_{dp} and Z_h values adopt the following form:

$$R = 15.693 K_{dp}^{0.780} \tag{7}$$

$$Z_h = 401.82 R^{1.575} \tag{8}$$

It must be mentioned that the way of fitting the parameters has a significant influence on the fitting parameters: As seen in Fig. 2, the density of the point cloud for low rain rate values is much higher than for high rain rates, which leads to large biases of the fit in the region of high rain rates. In order to overcome this effect, the rain rate was separated into different bins that contained an equal number (20) of Z_h or K_{dp} values, respectively. Hence for low rain rates, these bins were very small due to the high abundance of Z_h (K_{dp}) values in these conditions. For higher rain rates, the bins consequently grew to

AMTD
5, 1717–1761, 2012

much larger widths. Finally, in order to obtain Eqs. (7) and (8), the center of these rain rate bins, $\bar{R}$, and the average of Z_h (K_{dp}) values within these bins, $\bar{Z}_h$ ($\bar{K}_{dp}$), were used for the fitting procedure instead of the original values. Nevertheless, relatively large errors in the estimation of R are introduced if the relations (Eqs. 7, 8) are used: We have found a standard deviation of $\sigma_R^{Z_h} = 23.6\,\mathrm{mm\,h^{-1}}$ and a bias (retrieved minus true rain rate) of $\Delta_R^{Z_h} = -1.67\,\mathrm{mm\,h^{-1}}$ if relation (Eq. 8) is used. The corresponding values for relation (Eq. 7) are $\sigma_R^{K_{dp}} = 13.8\,\mathrm{mm\,h^{-1}}$ and $\Delta_R^{K_{dp}} = -0.599\,\mathrm{mm\,h^{-1}}$.

4 The extended Kalman filter algorithm

In Schneebeli and Berne (2012), a method for the processing of polarimetric X-band radar data based on an extended Kalman filter was presented. With this method it is possible to correct X-band radar measurements for attenuation and differential attenuation caused by the rain medium but also to estimate the reflectivity offset that might be induced by a wet radome or by a mis-calibration of the radar. In addition, the total differential phase shift measured by the radar Ψ_{dp} can be separated into the differential phase shift on propagation Φ_{dp} and on backscatter δ_{hv}, while the sum of the two equals Ψ_{dp} without the measurement noise.

The extended Kalman filter (EKF) method employs relations between different polarimetric moments and relations of these moments between one range gate and the upcoming one, as well as covariances associated with these relations in order to constrain the solution space of the attenuation corrected reflectivities and the de-noised differential phase measurements. Relations between polarimetric moments are established with DSD measurement from Parsivel disdrometers and subsequent T-matrix modeling of polarimetric parameters. For the EKF method to work, the parameters $\mu_{h,v}$, $\kappa_{h,v}$, $\lambda_{h,v}$, ζ and η for the following relations must be found (for details the reader is referred to Schneebeli and Berne, 2012):

$$\Psi_{dp}(i) = -2\Delta r 10^{\tilde{K}_{dp}(i)/10} + \Phi'_{dp}(i) + \delta_{hv}(i) \quad (9)$$

AMTD
5, 1717–1761, 2012

$$\Psi_{dp}(i+1) = 2\Delta r 10^{\tilde{K}_{dp}(i)/10} + \Phi_{dp}(i) + \delta_{hv}(i) \quad (10)$$

$$\tilde{Z}_h^m(i) = \mu_h \Phi_{dp}(i) + \tilde{Z}_h(i) \quad (11)$$

$$\tilde{Z}_v^m(i) = \mu_v \Phi_{dp}(i) + \tilde{Z}_v(i) \quad (12)$$

$$\kappa_h = \lambda_h \tilde{K}_{dp}(i) - \tilde{Z}_h(i) \quad (13)$$

$$\kappa_v = \lambda_v \tilde{K}_{dp}(i) - \tilde{Z}_v(i) \quad (14)$$

$$0 = \zeta \left(\tilde{Z}_h(i) - \tilde{Z}_v(i) \right)^{\eta} - \delta_{hv}(i) \quad (15)$$

$$0 = \Phi'_{dp}(i) - \Phi_{dp}(i) - 2\Delta r 10^{\tilde{K}_{dp}(i)/10} \quad (16)$$

In the above equations, the range resolution is written as Δr, Z_h^m and Z_v^m are the measured reflectivities at h and v polarization, respectively. Quantities that are expressed in dB are denoted with a $\sim$ and i is the range gate number. In addition the notation $\Phi'_{dp}(i) = \Phi_{dp}(i+1)$ was introduced in order to overcome ambiguities in the notation.

The parameters for the above equations are given in Table 2. They were deduced from the modeling results that are shown in Fig. 5. A similar procedure for the fitting of the polarimetric observables as described in the foregoing section was employed in order to increase the weighting of the (usually few) high values in the fitting process.

The EKF method not only employs the relations given in Eqs. (9)–(16) as well as the covariance associated with these relations, it also makes use of the knowledge of the spatial variability of the polarimetric moments. Since it was found that the results of the EKF algorithm are not very sensitive to possible errors in the spatial representation to the polarimetric moments, spatial DSD data from Switzerland were used in order to calculate the gate-to-gate variability of the polarimetric observables. This data was obtained from a DSD simulator that is able to produce realistic spatial DSD fields (Schleiss et al., 2009) and hence delivers information on the spatial behavior of the

AMTD
5, 1717–1761, 2012

polarimetric moments within a rain cell. This simulator was however constrained with spatial DSD measurements of Switzerland that are not necessarily representative for the locations in Brazil and it can also not be easily adapted to the different spatial DSD characteristics at the two locations.

One of the advantages of the EKF scheme lies in the fact that it can also be used to correct reflectivity offsets that are caused, for example, by a wet radome. Since the EKF scheme intrinsically calculates K_{dp} and Φ_{dp}, the two variables resulting from EKF calculations with different reflectivity offsets can be compared along one ray path and the comparison that exhibits the smallest absolute bias determines the reflectivity offset. This approach is somehow similar to the methods adopted in the so-called "self-consistency" attenuation correction algorithms (Bringi et al., 2001; Gorgucci et al., 2006). In Fig. 3, an example is given on how this algorithm works: In panel (a) three pairs of $\int 2K_{dp}dx$ and Φ_{dp} profiles that were inferred with the EKF algorithm are shown. The only difference between the pairs of profiles is the initial reflectivity offset (indicated at the beginning of the range profiles) that was added to the measured reflectivity prior to the treatment with the EKF algorithm. It is seen that a reflectivity offset of 10 dBZ leads to the smallest bias between the curve pairs compared to the two other offsets (5 and 15 dBZ). In panel (b), the absolute bias between the curve pairs is plotted against the initial reflectivity offset. The minimum of the curve shown in this plot (around 10 dBZ) determines the final radar reflectivity offset.

In Fig. 4, an example for the performance of the EKF and the ZPHI algorithm is given. In this plot, the original (offset corrected) reflectivity and differential reflectivity together with the attenuation corrected reflectivities as a function of the radar range are depicted. In addition, K_{dp} inferred from the EKF scheme as well as the original measured differential phase together with the EKF calculated Φ_{dp} and δ_{hv} are shown. It is seen that the two attenuation correction schemes exhibit a considerable bias at the end of the range profile and it is not yet clear what is causing this difference. However, in panel (d) it is seen that δ_{hv} and Φ_{dp} add up nicely to the measured phase Ψ_{dp}, which is a good indication that the algorithm performs well.

AMTD
5, 1717–1761, 2012

5 Attenuation correction with ZPHI

In order to compensate the energy loss due to extinction and attenuation the radar beam suffers when it propagates through the rain medium the well known ZPHI algorithm (Testud et al., 2000) was implemented. With this method, attenuation and differential attenuation is calculated as

$$A_h(i) = \frac{Z_h(i)^b}{I(0,i_1) + \left(10^{0.1b\gamma\Delta\Phi_{dp}} - 1\right) I(i,i_1)} \times \left(10^{0.1b\gamma\Delta\Phi_{dp}} - 1\right) \quad (17)$$

$$A_{dp} = \alpha A_h^{\beta} \quad (18)$$

with

$$I(i,i_1) = 0.46b \sum_{j=i}^{i_1} Z_h(j)^b \Delta r \quad (19)$$

Hereby, i_1 is the last gate of the range profile, $\Delta\Phi_{dp}$ is the differential phase from 0 to i_1, b is defined as the exponent of the relation

$$A_h(i) = xZ_h(i)^b \quad (20)$$

and γ stems from the relation

$$A_h(i) = \gamma K_{dp}(i). \quad (21)$$

The performance of ZPHI solely depends on the accuracy of the estimation of the b, β, α and γ parameters. These parameters were calculated as described in the foregoing section by applying the T-matrix method to DSDs measured with a disdrometer. The calculations corresponding to the relations of Eqs. (20) and (21) are shown

AMTD
5, 1717–1761, 2012

in Fig. 5d, b, respectively. Also note that the parameter γ given in Eq. (21) is similar to the parameter μ in Eq. (11).

The numerical values of the determined parameters are given in Table 3.

6 Differential reflectivity bias correction

In addition to the reflectivity offset, there exists also a bias in Z_{dr} that needs to be removed before the data can be further processed. Traditionally, this offset is determined by pointing the antenna in vertical direction and rotating it around the azimuthal axis (Seliga et al., 1979; Gorgucci et al., 1999). Since the rain drops at this incidence angle should not exhibit any differential polarization, the Z_{dr} data that is acquired in this manner can be averaged (over the range gates and the azimuthal angles), which should lead to a value that corresponds to the difference between the H- and the V-channel. Probably due to the damaged radome, the Z_{dr} offset shows a distinct dependence on the azimuth angle as it is seen in Fig. 6a. As stated in Gorgucci et al. (1999), this azimuthal dependence hampers the applicability of the Z_{dr} calibration procedure with the rotating antenna.

In Fig. 6b it is seen that the Z_{dr} offset is relatively stable in time (with just some outliers that are probably due to atmospheric effects like partial beam filling at the end or the beginning of a rain event). It is therefore suggested to determine the Z_{dr} offset just once or only from time to time and then assume the offset to be stable over time. At the moment we believe that with this procedure more accurate Z_{dr} values can be obtained than with a regular offset correction.

Because of the aforementioned issues, Z_{dr} needs to be calibrated with a method that does not rely on data gathered at vertical incidence. If the antenna points at a horizontal direction into a rain field, Z_{dr} values are usually unknown apriori and can therefore not be used to calibrate the radar. There is however one exception: if the reflectivity values are low and the data is not affected by attenuation, then the Z_{dr} values have to be very close to zero. This assumption was tested with T-matrix simulations

AMTD
5, 1717–1761, 2012

and the mean and standard deviation of Z_{dr} in such low reflectivity conditions was calculated to a value of $Z_{dr} = 0.1 \pm 0.052$ dB. If it is now possible to find such values (low Z_h, no attenuation), the corresponding Z_{dr} values can be set to $Z_{dr}^{low} = 0.10$ which determines the Z_{dr} offset. To do so, it was searched for these conditions by applying certain criteria: First, the Z_h values had to be low and fulfill the condition $0\,\mathrm{dBZ} \leq Z_h \leq 10\,\mathrm{dBZ}$. A lower reflectivity limit was set in order to reduce noise that is due to low signal-to-noise ratios (the raw power measurements were not stored, hence a threshold on the signal power could not be applied). Second, only values in regions where the sum of Z_h along a ray profile did not exceed 200 dBZ were considered. This threshold ensured that Z_{dr} values only suffered from little attenuation. In Fig. 7 a histogram of Z_{dr} found in these conditions is shown. Data used for this figure were collected on 12 April 2011. With the mean value of $Z_{dr} = 0.34$ dB, we can determine the Z_{dr} offset to $Z_{dr}^{off} = 0.34\,\mathrm{dB} - Z_{dr}^{low} = 0.24$ dB. Although other methods exist in the literature to determine the Z_{dr} offset without pointing to zenith direction (Ryzhkov et al., 2005; Bechini et al., 2008), these methods require stratiform precipitation while during our campaign mostly convective situations were encountered.

Due to the relatively large standard deviation of $\sigma_{Z_{dr}} = 1.31$ dB that is found in the histogram, it is questionable if this method is accurate enough for calibrating Z_{dr}. This high standard deviation is most likely induced by very low reflectivities that exhibit a low signal-to-noise ratio. It could however also be caused by polarization leakage effects (Wang and Chandrasekar, 2006) that can lead to considerable biases in Z_{dr} (up to 1 dB). Especially simultaneously transmitting radars like the one that is employed in the study at hand are prone to such errors in Z_{dr}.

AMTD
5, 1717–1761, 2012

7 Results and discussion

7.1 Reflectivity offset due to radome attenuation

In Sect. 4 it was shown how the reflectivity offset due to mis-calibration and/or radome effects can be determined with the EKF method. However, a minimal total differential phase shift (Φ_{dp}^{max}) of 20° along the radar ray path is necessary for the method to work properly, such that the calibration offset can be determined accurately. It is very common that Φ_{dp}^{max} is below the proposed threshold and then the radome offset has to be determined differently, which is detailed in the following: from Fig. 5 it is seen that there is a close relation between the reflectivity $\tilde{Z}_{h,v}$ and $\tilde{K}_{dp}$. If Φ_{dp}^{max} along a ray path is low, i.e. if the reflecivities along this path only suffer from low attenuation, this relation can be used to determine the reflectivity offset by calculating $\tilde{Z}_{h,v}$ from $\tilde{K}_{dp}$ employing the relations given in Eqs. (13) and (14) and then comparing the results to the measured reflectivities $\tilde{Z}_{h,v}^{m}$. This method, which will be called "K_{dp} method" in the following, is employed where $\Phi_{dp}^{max} < 20°$. Due to the large scatter that is inherent in the relations of Eqs. (13) and (14), the K_{dp} method is expected to provide less accurate estimates of the reflectivity offset than the EKF method. Attenuation effects that can negatively influence the K_{dp} method are overcome by applying ZPHI attenuation correction to the reflectivities prior to determining the reflectivity offset. Also note that the K_{dp} method depends on the elevation angle due to the elevation dependence of K_{dp}. Since this method is applied only for elevation angles $\phi < 6°$, this dependence is negligible and hence no specific elevation angle correction was applied.

In order to get an example of the variability of the reflectivity offset, the radome attenuation has been determined in azimuth and elevation direction for 12 April 2011, 05:20 UTC and the result is given in Fig. 8, where the reflectivity offset as a function of the azimuth angle is shown in panel (a) and as a function of the elevation angle in panel (b). At the time of the observation, very intense rainfall was encountered right above the radar. In panel (a), only the EKF method was employed to compile the plot in

AMTD
5, 1717–1761, 2012

order to eliminate the influence of the choice of the method on the result. No offset was calculated for directions where a value of $\Phi_{dp}^{max} = 20^{\circ}$ could not be reached, and in the graphical representation the values in these regions were simply interpolated linearly.

The plot in panel (b) is differently compiled: Since the EKF method was developed for horizontal incidence of the radar beam to the rain drops, the relations given in Eqs. (9)–(15) are not valid anymore for too high elevation angles. T-matrix simulations showed that the difference between an elevation angle of 45° and 0° leads to biases in the EKF parameters (given in Table 2) of up to 100 % (for the $\mu_{h,v}$ parameters), which is not acceptable for the scope of the application. Hence, the EKF parameters had to be corrected for higher elevation angles with a procedure that is detailed in Appendix A. For elevation angles higher than 45°, the EKF method becomes inaccurate although the parameters were elevation angle corrected, since the polarimetric signature of the rain vanishes with increasing elevation angle. Therefore, the EKF method was employed for the calculation of the reflectivity offset only up to an elevation angle of 45°. The values for higher angles were interpolated with the assumption that the reflectivity at the first range gate for elevation angles of 45° to 135° is constant due to the low spatial extent of the volume that is defined with these conditions. If the assumption of the constant reflectivity right above the radar is true, then the reflectivity offset for the high elevation angles can be deduced from the reflectivity offset at 45° elevation calculated with the EKF method and the measured reflectivity at the first range gate from this direction. The result of this procedure is shown in Fig. 8b, where the reflectivity offsets determined with the EKF method are plotted in black and those interpolated with the method described above are plotted in grey.

It is seen that around 110° elevation, a local maximum of the radome attenuation is encountered. It is very likely that this maximum is caused by the damaged radome that was fixed with fiberglass and glue, since the damage is located in the direction where the attenuation maximum is encountered. Apparently, the performance of the fixed radome in terms of transparency is slightly worse than the undisturbed radome. However, the most striking feature in this graph are the high values around 18 dB that

AMTD
5, 1717–1761, 2012

were measured for the reflectivity offset. These measurements emphasize that the radar data without radome correction cannot be used for any quantitative analysis if the radome is under influence of heavy rain.

In azimuth direction, it is seen that the variation of the offset is relatively large, ranging from 16.5 to 20 dB (with one orientation that exhibits a value of 22 dB). The variability in azimuth could be related to non uniform wetting or non uniform drying of the radome, which is probably caused by wind patterns. Due to this high variability, it is not recommended to apply a general correction that is valid for all the azimuthal directions. In order to get observations of high quality and maximum accuracy, every direction should be individually corrected for radome induced offsets.

In Bechini et al. (2010) a function is reported that links the radome attenuation of the same Gematronik X-band radar with the rain intensity that was measured at the radar location. This function for the radome attenuation L_{rad} reads:

$$L_{\mathrm{rad}} = 2\left(-0.34 + 1.75R^{1/3}\right) \tag{22}$$

with the rain rate R [mm] and L_{rad} in [dB]. Unfortunately, we did not deploy an instrument to measure R at the radar site, which makes it a bit more difficult to compare our findings with Eq. (22). In order to estimate R at the radar site, the offset corrected reflectivity data from the first range gates when the antenna pointed at vertical direction were taken and averaged. Then, R was estimated with the Z–R relation given in Eq. (8) that was found from the T-matrix simulations shown in Fig. 5. The reflectivity offsets determined with the two different methods are shown as a scatter plot in Fig. 9.

It is seen that where the Bechini method estimates higher offset values ($\Delta Z_{\mathrm{h}} > 5$ dB), a clear correlation between the two methods is observed with the EKF method providing slightly higher offset estimates. Where the Bechini method indicates a low offset, the scatter between the two methods is very high and it is difficult to see any correlation at all. The reason of this behavior is found in the fact that the radome can remain wet even when it is not raining right at the location of the radar. In this case, i.e. if the radome is still wet but the rain intensity is zero, the Bechini method also estimates the

AMTD
5, 1717–1761, 2012

radome offset to zero. Another error source of the Bechini method is the imperfection of the R estimation due to the scatter of the $Z-R$ relationship. However, if the rain rate were estimated directly at the radar site with a pluvio- or disdrometer, this error could be mitigated. The Bechini method also only estimates the reflectivity offset due to the wet radome. Any calibration effects that are caused by a different effect (e.g. variations in the receiver sensitivity, variations in the transmitted power, errors in the estimation of the radar constant) cannot be tackled with this method and are therefore expected to contribute to the scatter as well as the bias found in Fig. 9a.

There is not only considerable variation of the radome offset in azimuth and elevation direction, but also in time, as it is seen in Fig. 9b, where a time series of the reflectivity offset determined in one single direction is plotted. For this plot, the K_{dp} method was employed where the EKF method could not be applied. It is seen that the reflectivity offset values determined with the EKF method are generally higher, since high values of $\Phi_{dp}^{max} \leq 20^{\circ}$, being a prerequisite for the EKF method to work, are more likely to be fond where also the rain intensity above the radar is high, i.e. where the radome is wet and therefore induces high signal attenuation. However, this is only a general rule, since it is possible to have a large Φ_{dp}^{max} in one direction even if the radar is located outside of a rain cell.

We can also use the whole data set that was corrected for radome attenuation to check if the radar manufacturer properly calibrated the radar for dry radome conditions. To do so, the assumption is made that the lowest reflectivity offset values correspond to conditions where the radome was dry. The 1 % quantile of all the reflectivity offset values is determined to $q_{0.01}^{\Delta Z} = -0.035\,\mathrm{dB}$ and for the 2 % quantile a value of $q_{0.02}^{\Delta Z} = 0.085\,\mathrm{dB}$ is found. These values show that the radar constant was determined accurately and hence the radar is well calibrated.

7.2 Rain attenuation correction

With the parameters given in Table 3 and the Eqs. (17) and (18), the attenuation A_h and differential attenuation A_{dp} can be calculated at every range gate along a ray path.

AMTD
5, 1717–1761, 2012

Together with the radome offset correction and the Z_{dr} offset correction, the data that are treated in this manner can be regarded as fully corrected and are ready for further scientific or operational use.

In Fig. 10, the polarimetric variables of one PPI scan that underwent the full data preprocessing chain is shown. Attenuation correction was performed with the ZPHI algorithm and K_{dp} stems from the EKF algorithm. The copolar correlation coefficient ρ_{hv} did not undergo any pre-processing and is taken as provided by the Gematronik radar.

In the shown reflectivity and differential reflectivity data, there remain still certain radial "streaks", especially in the directions West and South of the radar. These streaks indicate that the radome offset correction in that specific direction was determined with low accuracy which causes inconsistencies in the Z_h and Z_{dr} field from one direction to the other. Discrepancies that can cause these streaks are numerous: It is possible that the method for determining the reflectivity offset changes from one azimuthal direction to the neighboring one from the EKF method to the K_{dp} method or vice versa. Partial beam blockage caused by ground clutter is expected to hamper the accuracy of the EKF method, since this effect causes the relations given in Eqs. (9)–(16) to become invalid or at least erroneous which has a negative effect on the accuracy of the determination of the reflectivity offset as a consequence. However, the general visual impression of the reflectivity fields suggest that the attenuation correction procedure leads to meaningful results and one must keep in mind that also ZPHI and any self-consistency methods would be degraded by partial beam blockage.

A further and rather extreme example that illustrates the necessity of radome and rain attenuation is shown in the Fig. 11: in panel (b) of this figure, which shows the reflectivity after all the pre-processing steps, it can be seen that a very strong rain cell is located right at the radar location. This rain cell causes very strong radome attenuation and hence the uncorrected data as shown in panel (a) differs considerably from the corrected one.

AMTD
5, 1717–1761, 2012

7.3 Comparisons with a disdrometer

The algorithm's performance can be quantitativley analyzed by comparing the corrected radar polarimetric moments with such moments that are modeled from DSD measurements of a Parsivel disdrometer located in a distance of 20 km to the radar. To do so, from the RHI scan that was performed in the disdrometer's azimuthal direction (316.7°), the corresponding range gate was extracted for an elevation angle of 2.5°. This angle corresponded to the lowermost elevation that was completely unspoiled from ground clutter contamination.

The polarimetric moments Z_h, Z_{dr} and K_{dp} inferred from the disdrometer DSD measurements were calculated according to the procedure detailed in Sect. 3 and compared to the attenuation corrected radar measurements. The reflectivity offset was calculated with the EKF method where applicable and with the K_{dp} method for the remaining cases. The EKF algorithm was also used to determine rain attenuation corrected Z_{dr} and Z_h as well as K_{dp} values. In addition, Z_h and Z_{dr} were also corrected for rain attenuation with the ZPHI method and K_{dp} was determined with the traditional algorithm of Hubbert and Bringi (1995) in order to assess the performance of the different methods.

In Fig. 12, a scatter plot with the horizontal reflectivity inferred from Parsivel data versus the uncorrected and corrected radar measurements is shown, where the radar measurements were corrected with the EKF algorithm. Since two methods for the correction of the reflectivity offset were employed, the corrected radar measurements are represented with a "∘" where the offset was deduced with the EKF method and with an "×" where the K_{dp} method was employed. Similarly to the findings in the previous section, the reflectivity offset associated with high Z_h values is usually determined with the EKF method, since it is likely to have high Φ_{dp}^{max} values during intense precipitation above the radar.

It is seen in the scatter plot that uncorrected reflectivities exhibit a considerable bias and that the attenuation correction (for both the radome and the rain medium) seem

AMTD
5, 1717–1761, 2012

to perform well. A statistical analysis of the performance of the correction schemes is given in Table 4, where also the performance of the ZPHI algorithm is evaluated. From this analysis, it is concluded that the ZPHI method, applied on radome attenuation corrected data, leads to the most stable reflectivity estimates with a reflectivity bias of $\Delta_{Z_h} = 0.759$ dB and a standard deviation of $\sigma_{Z_h} = 8.49$ dB. Attenuation correction with the EKF algorithm is slightly less accurate ($\Delta_{Z_h} = 1.64$ dBZ, $\sigma_{Z_h} = 8.75$ dB). Given the large bias of the completely uncorrected data ($\Delta_{Z_h} = 14.6$ dBZ) and regarding other effects like the spatial variability of the DSD within a radar resolution volume (Jaffrain and Berne, 2011), the performance of both, ZPHI and EKF, lead to an acceptable residual bias.

Figure 13 shows the same than in Fig. 12 but for the differential reflectivity Z_{dr}. The offset in Z_{dr} determined in Sect. 6 was added to the measured Z_{dr} values before the data were further treated with the EKF algorithm and the ZPHI method. Similar to the findings for Z_h, it is seen that uncorrected Z_{dr} data can exhibit a large error and that the attenuation correction with the EKF method performs reasonably. Again, the statistical evaluation is found in Table 4.

While the bias in Z_{dr} is similar for EKF and ZPHI ($\Delta_{Z_{dr}} \approx -0.21$ dB), a slightly better standard deviation is found for EKF ($\sigma_{Z_{dr}} = 0.59$ dB) than for ZPHI ($\sigma_{Z_{dr}} = 0.71$ dB). The reason is found in Fig. 4, where it can be seen that Z_{dr} data treated with the EKF algorithm are less noisy than the raw or ZPHI treated data. Apparently, this noise reduction not only has a positive effect on $\sigma_{Z_{dr}}$, but also the correlation coefficient $R^2_{Z_{dr}}$ between the disdrometer and the radar values is distinctly enhanced compared to ZPHI or raw data.

Finally, the same analysis as for Z_{dr} and Z_h was performed for K_{dp} and the result is shown in Fig. 14. Since K_{dp} is a quantity that is not directly measured, the values inferred from the EKF method were compared to data deduced with the algorithm of Hubbert and Bringi (1995), which is based on a smoothing procedure and a subsequent derivation of the measured differential phase Ψ_{dp}. This algorithm was already implemented in the radar's data analysis software and the data were taken as provided

AMTD
5, 1717–1761, 2012

without further change. In conditions of high K_{dp}, the EKF algorithm seems to provide slightly underestimated values, while in conditions of low K_{dp}, the algorithm of Hubbert and Bringi (1995) provides too high K_{dp} estimates. Overall it is seen in Table 4 that K_{dp} estimated with EKF outperform the traditional K_{dp} estimates inferred from the algorithm of Hubbert and Bringi (1995) in terms of bias, standard deviation and correlation.

8 Conclusions

Polarimetric X-band radar data were collected in in Fortaleza, northern Brazil. It was found that the reflectivity is heavily affected by attenuation of the radome and the rain medium itself. An extended Kalman filter algorithm capable of radome and rain attenuation correction was implemented and data from one month was processed. The radome attenuation in azimuth and elevation direction was not found to be constant within one scan, hence it is recommended to correct every direction independently. In addition to the EKF algorithm, a standard rain attenuation correction scheme (ZPHI) was implemented. The necessary adaptations of this scheme, i.e. the proper calculation of attenuation parameters, were performed with modeled polarimetric observables that are based on DSDs measured with three Parsivel disdrometers. The corrected X-band radar measurements were compared with the disdrometer measurement located in 20 km distance from the radar. This comparison showed that the implemented algorithms performed satisfactory: reflectivities corrected with ZPHI exhibited the smallest bias and standard deviation compared to the disdrometer data as well as the highest correlation, the EKF algorithm outperformed ZPHI in the correction of the differential reflectivities. The EKF method was also found to give better estimates of K_{dp} than the algorithm of Hubbert and Bringi (1995). Given the large biases of uncorrected data, it must be emphasized that without radome attenuation correction such accurate estimates would not have been possible. It was also shown that the variability of the reflectivity offset in direction and time is extremely variable, hence it is strongly recommended to implement a radome attenuation correction scheme that individually

AMTD
5, 1717–1761, 2012

corrects for every direction and at every time step. The correction of rain attenuation at X-band frequencies by employing polarimetric techniques is meanwhile a standard procedure. The results of this study suggest that also the correction of radome attenuation should become part of a standard X-band weather radar data processing scheme.

Appendix A

Elevation angle correction for EKF parameters

The parameters for the EKF algorithm given in Table 2 were calculated for an elevation angle of $\Theta = 0^\circ$ and are therefore denoted as P_0^{EKF}. For higher elevation angles, these parameters are subject to a slight change, which might influence the performance of the EKF retrieval. In order to mitigate these possible errors, the EKF parameters were calculated for elevation angles of $0^\circ \geq \Theta \leq 45^\circ$ with a 5° interval. From these calculations, correction functions of the form

$$P_\Theta^{\mathrm{EKF}} = P_0^{\mathrm{EKF}} + f\Theta^g \tag{A1}$$

where Θ is in [deg] and f and g are power law coefficients that were determined from linear least square fits on the logarithm of Θ and the logarithm of $P_\Theta^{\mathrm{EKF}} - P_0^{\mathrm{EKF}}$. The coefficients f and g are given in Table 1 for every EKF parameter.

Acknowledgements. This work is supported by FAPESP grant No. 2009/15235-8. Without the expertise of Cesar de Mello in deploying the radar and making it work as well as the effort of Jorge Luiz Marton, Jorge Mello and Jorge Nogueira in setting up the various other instruments, this campaign would not have taken place. We also thank Meiry Sayuri Sakamoto for hosting us at FUNCEME and for her great support in conducting the campaign in Fortaleza.

AMTD
5, 1717–1761, 2012

References

Anagnostou, E. N., Anagnostou, M. N., Krajewski, W. F., Kruger, A., and Miriovsky, B. J.: High-resolution rainfall estimation from X-band polarimetric radar measurements, J. Hydrometeorol., 5, 110–128, 2004. 1718

Anagnostou, E. N., Grecu, M., and Anagnostou, M. N.: X-band polarimetric radar rainfall measurements in Keys area microphysics project, J. Atmos. Sci., 63, 187–203, 2006. 1719

Andsager, K., Beard, K. V., and Laird, N. E.: Laboratory measurements of axis ratios for large raindrops, J. Atmos. Sci., 56, 2673–2683, 1999. 1723

Barber, P. and Yeh, C.: Scattering of electromagnetic waves by arbitrarily shaped dielectric bodies, Appl. Opt., 14, 2864–2872, 1976. 1723

Battaglia, A., Rusemeyer, E., Tokay, A., Blahak, U., and Simmer, C.: PARSIVEL snow observations: a critical assessment, J. Atmos. Ocean. Techn. , 27, 333–344, 2010. 1722

Bechini, R., Baldini, L., Cremonini, R., and Gorgucci, E.: Differential Reflectivity Calibration for Operational Radars, J. Atmos. Ocean. Tech., 25, 1542–1555, 2008. 1730

Bechini, R., Chandrasekar, V., Cremonini, R., and Lim, S.: Radome attenuation at X-band radar operations, in: Proc. 6th European Conf. on Radar in Meteorology and Hydrology: Adv. in Radar Technology, Sibiu, Romania, 2010. 1719, 1733, 1756

Berne, A., Delrieu, G., and Andrieu, H.: Estimating the vertical structure of intense Mediterranean precipitation using two X-band weather radar systems, J. Atmos. Ocean. Techn., 22, 1656–1675, 2005. 1719

Brandes, E., Zhang, G., and Vivekanandan, J.: Experiments in rainfall estimation with a polarimetric radar in a subtropical environment, J. Appl. Meteorol., 41, 674–685, 2002. 1723

Bringi, V. N. and Chandrasekar, V.: Polarimetric Doppler Weather Radar: Principles and Applications, Cambridge University Press, 2001. 1723

Bringi, V. N., Keenan, T. D., and Chandrasekar, V.: Correcting C-Band radar reflectivity and differential reflectivity data for rain attenuation: a self-consistent method with constraints, IEEE T. Geosci. Remote, 39, 1906–1915, 2001. 1727

Delrieu, G., Serrar, S., Guardo, E., and Creutin, J.-D.: Rain measurement in hilly terrain with X-band weather radar systems: accuracy of path-integrated attenuation estimates derived from mountain return, J. Atmos. Ocean. Tech., 16, 405–415, 1999. 1718

Gorgucci, E., Scarchilli, G., and Chandrasekar, V.: A procedure to calibrate multiparameter weather radar using properties of the rain medium, IEEE T. Geosci. Remote, 37, 269–276,

AMTD
5, 1717–1761, 2012

1999. 1729
Gorgucci, E., Chandrasekar, V., and Baldini, L.: Correction of X-band radar observation for propagation effects based on the self-consistency principle, J. Atmos. Ocean. Tech., 23, 1668–1681, 2006. 1718, 1727
Hubbert, J. and Bringi, V. N.: An iterative filtering technique for the analysis of copolar differential phase and dual-frequency radar measurements, J. Atmos. Ocean. Tech, 12, 643–648, 1995. 1720, 1736, 1737, 1738, 1751, 1761
Jaffrain, J. and Berne, A.: Experimental Quantification of the Sampling Uncertainty Associated with Measurements from PARSIVEL Disdrometers, J. Hydrometeorol., 12, 352–370, 2011. 1722, 1737
Matrosov, S. Y.: Evaluating polarimetric X-band radar rainfall estimators during HMT, J. Atmos. Ocean. Tech., 27, 122–134, 2010. 1719
McLaughlin, D., Pepyne, D., Chandrasekar, V., Philips, B., Kurose, J., Zink, M., Droegemeier, K., Cruz-Pol, S., Junyent, F., Brotzge, J., Westbrook, D., Bharadwaj, N., Wang, Y., Lyons, E., Hondl, K., Liu, Y., Knapp, E., Xue, M., Hopf, A., Kloesel, K., Defonzo, A., Kollias, P., Brewster, K., Contreras, R., Dolan, B., Djaferis, T., Insanic, E., Frasier, S., and Carr, F.: Short-wavelength technology and the potential for distributed networks of small radar systems, B. Am. Meteorol. Soc., 90, 1797–1817, 2009. 1718
Meissner, T. and Wentz, F. J.: The complex dielectric constant of pure and sea water from microwave satellite observations, IEEE T. Geosci. Remote, 42, 1836–1849, 2004. 1723
Mishchenko, M. I. and Travis, L. D.: Capabilities and limitations of a current FORTRAN implementation of the T-matrix method for randomly oriented, rotationally symmetric scatterers, J. Quant. Spectrosc. Ra., 60, 309–324, 1998. 1720, 1723
Peters, G., Fischer, B., and Andersson, T.: Rain observations with a vertically looking Micro Rain Radar (MRR), Boreal Environ. Res., 7, 353–362, 2002. 1719
Ryzhkov, V. R., Giangrande, S. E., Melnikov, V. M., and Schuur, T. J.: Calibration issues of dual-polarization radar measurements, J. Atmos. Ocean. Tech., 22, 1138–1155, 2005. 1730
Schleiss, M., Berne, A., and Uijlenhoet, R.: Geostatistical simulation of 2D fields of raindrop size distributions at the meso-γ scale, Water Resour. Res., 45, W07415, doi:10.1029/2002RS002856, 2009. 1726
Schneebeli, M. and Berne, A.: An extended Kalman filter framework for polarimetric X-Band weather radar data processing, J. Atmos. Ocean. Tech., in press, doi:10.1175/JTECH-D-10-05053.1, 2012. 1720, 1725

AMTD
5, 1717–1761, 2012

Schneebeli, M., Berne, A., Jolivet, S., Muth, X., Jaffrain, J., Dawes, N., and Lehning, M.: Measurements of Alpine Precipitation with an X-Band Polarimetric Radar and Additional Sensors, in: Proc. 6th European Conf. on Radar in Meteorology and Hydrology: Adv. in Radar Technology, 6–10 September, Sibiu, Romania, 2010. 1719

Seliga, T. A., Bringi, V. N., and Al-Khatib, H. H.: Differential reflectivity measurements in rain: first experiments, IEEE T. Geosci. Remote, 17, 240–244, 1979. 1729

Testud, J., Bouar, E. L., Obligis, E., and Ali-Mehenni, M.: The rain profiling algorithm applied to polarimetric weather radar data, J. Atmos. Ocean. Techn., 17, 332–356, 2000. 1718, 1720, 1728

Thurai, M. and Bringi, V. N.: Drop axis ratios from a 2D video disdrometer, J. Atmos. Ocean. Techn., 22, 966–978, doi:10.1175/JTECH1767.1, 2005. 1723

Wang, Y. and Chandrasekar, V.: Polarization isolation requirements for linear dual-polarization weather radar in simultaneous transmission mode of operation, IEEE T. Geosci. Remote, 44, 2019–2028, 2006. 1730

Wang, Y. and Chandrasekar, V.: Quantitative precipitation estimation in the casa x-band dual-polarization radar network, J. Atmos. Ocean. Techn., 27, 1665–1676, 2010. 1718

Ware, R., Solheim, F., Carpenter, R., Güldner, J., Liljegren, J., Nehrkorn, T., and Vandenberghe, F.: A multi-channel radiometric profiler of temperature, humidity and cloud liquid, Radio Sci., 38, 8079, doi:10.1029/2002RS002856, 2003. 1719

Zrnic, D. S. and Ryzhkov, A. V.: Polarimetry for weather surveillance radars, B. Am. Meteorol. Soc., 80, 389–406, 1999. 1718

AMTD
5, 1717–1761, 2012

Table 1. Specifications of the Gematronik radar.

Transmitter	Magnetron delivering 35 kW per channel.
Polarization	Simultaneous horizontal and vertical transmission.
Pulses	Staggered PRF (pulse repetition frequency) mode with PRFs of 1200 Hz and 1500 Hz as well as ordinary pulse pair mode (PRF: 1500 Hz); pulse length of 0.5 µs (150 m resolution).
Antenna	1.8 m diameter, 1.3° 3-dB beam width.
Antenna gain	43 dB
Operating frequency	9.375 GHz
Scanning protocol	Combination of RHI and volume scans. See the Sect. 2.2 for details.
Pulse sampling	PPI scans: 68 samples per ray @ 1° angular resolution. RHI scans: 150 samples per ray @ 0.5° angular resolution.
Positioning	Sun tracking method.

AMTD
5, 1717–1761, 2012

Table 2. Parameters for the EKF method caluclated from the DSDs of three Parsivel disdrometers.

μ_h	μ_v	κ_h	κ_v	λ_h	λ_v	ζ	η
0.208	0.163	44.031	42.350	1.283	1.176	0.781	1.532

AMTD
5, 1717–1761, 2012

Table 3. Parameters for the the ZPHI attenuation correction method caluclated from the DSDs of three Parsivel disdrometers.

γ	b	α	β
0.208	0.687	0.117	1.265

AMTD
5, 1717–1761, 2012

Table 4. Standard deviation (std), bias and correlation coefficient between the polarimetric moments calculated from the DSD measurements and the corrected and raw radar measurements.

Observable	Bias			std			Correlation		
	EKF	ZPHI	raw	EKF	ZPHI	raw	EKF	ZPHI	raw
Z_h [dBZ]	1.64	0.759	14.644	8.75	8.49	10.59	0.785	0.802	0.719
Z_{dr} [dB]	−0.210	−0.214	−0.310	0.590	0.720	0.826	0.709	0.328	0.223
K_{dp} [° km^{-1}]	0.750	–	0.858	2.16	–	2.29	0.762	–	0.728

AMTD
5, 1717–1761, 2012

Table A1. Power law coefficients that are used to correct the EKF parameters for elevation angles $\Theta \neq 0$.

	μ_h	μ_v	κ_h	κ_v	λ_h	λ_v	ζ	η
f	1.40×10^{-4}	1.21×10^{-4}	2.86×10^{-3}	2.94×10^{-3}	2.19×10^{-5}	5.29×10^{-5}	4.90×10^{-5}	1.86×10^{-3}
g	1.77	1.80	1.85	1.90	1.72	1.89	2.19	0.97

AMTD
5, 1717–1761, 2012

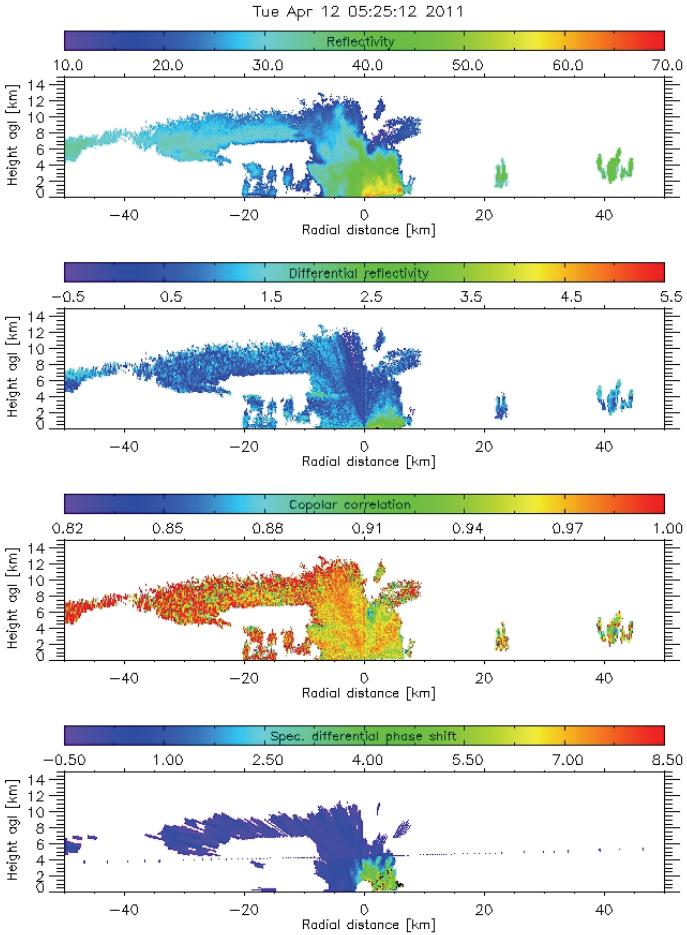

Fig. 1. Example of the polarimetric observables from one horizon-to-horizon RHI sweep performed on 12 April 2011 in Fortaleza.

AMTD
5, 1717–1761, 2012

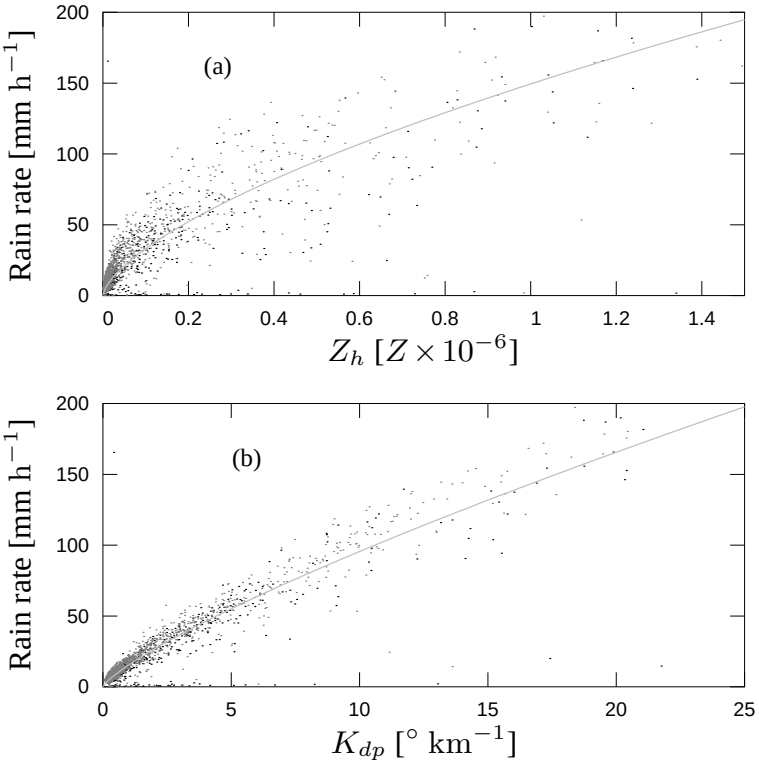

Fig. 2. **(a)** Scatterplot of the rain rate R versus the radar reflectivity Z_h based on disdrometer derived DSD measurements. **(b)** Same as in panel **(a)** but for the rain rate R versus K_{dp}. The values of the shown power law fits are given in Eqs. (8) and (7)

.

AMTD
5, 1717–1761, 2012

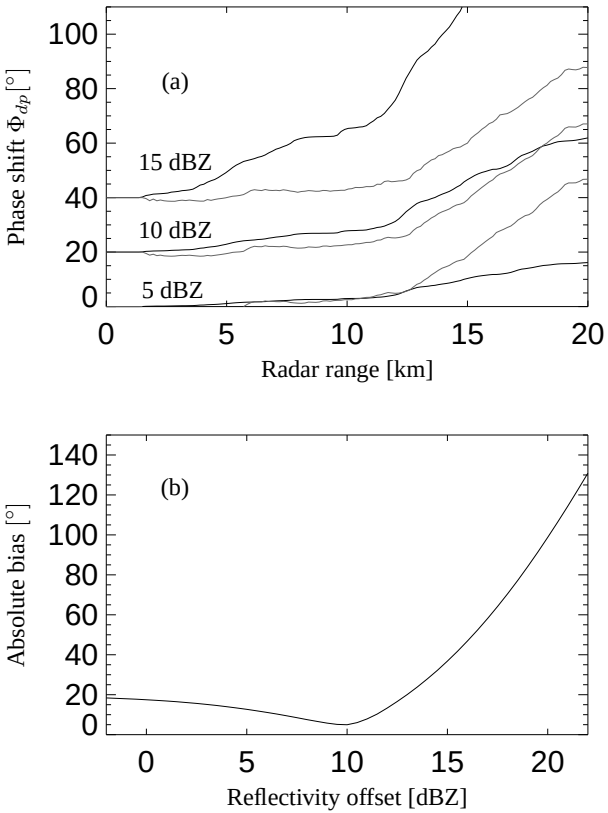

Fig. 3. (a) Range integrated K_{dp} (black lines) and Φ_{dp} (grey lines) both inferred from the EKF algorithm and calculated with three different reflectivity offsets. The three curves associated with the three reflectivity offsets are plotted with a phase offset of 20°. **(b)** The abolute bias between the black and the grey lines from the upper panel as a function of the reflectivity offset.

AMTD
5, 1717–1761, 2012

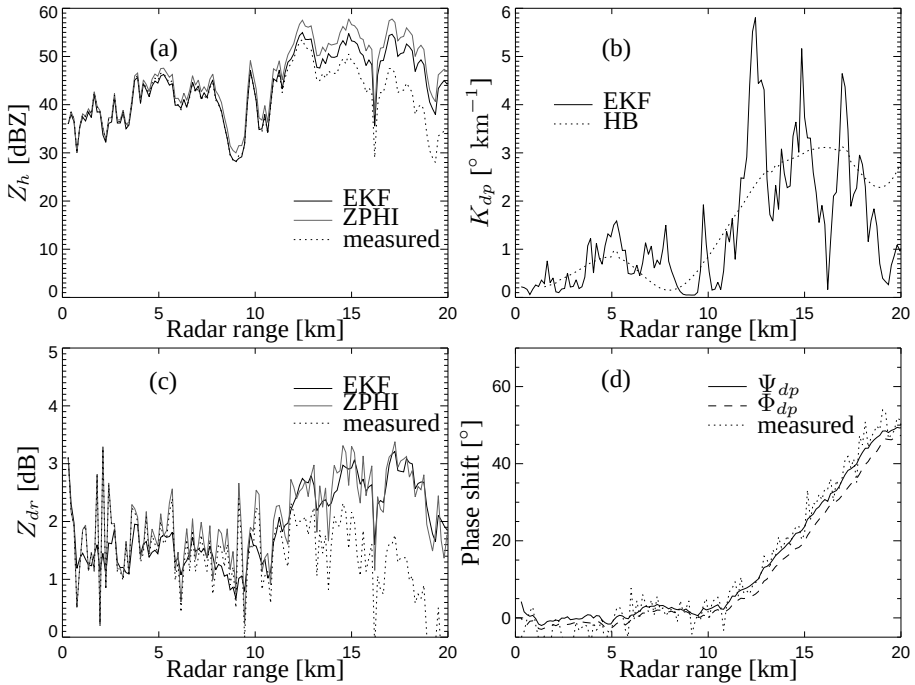

Fig. 4. **(a)** Profile of the measured (dotted) and attenuation corrected (ZPHI: grey line, EKF: black line) Z_h. **(b)** Ray profile of K_{dp} estimated with EKF and with the algorithm of Hubbert and Bringi (1995). **(c)** Same as in **(a)** but for Z_{dr}. **(d)** Ray profiles of the measured (dotted) and retrieved (black line) total differential phase Ψ_{dp}, which is the sum of the retrieved δ_{hv} and Φ_{dp} (dashed).

AMTD
5, 1717–1761, 2012

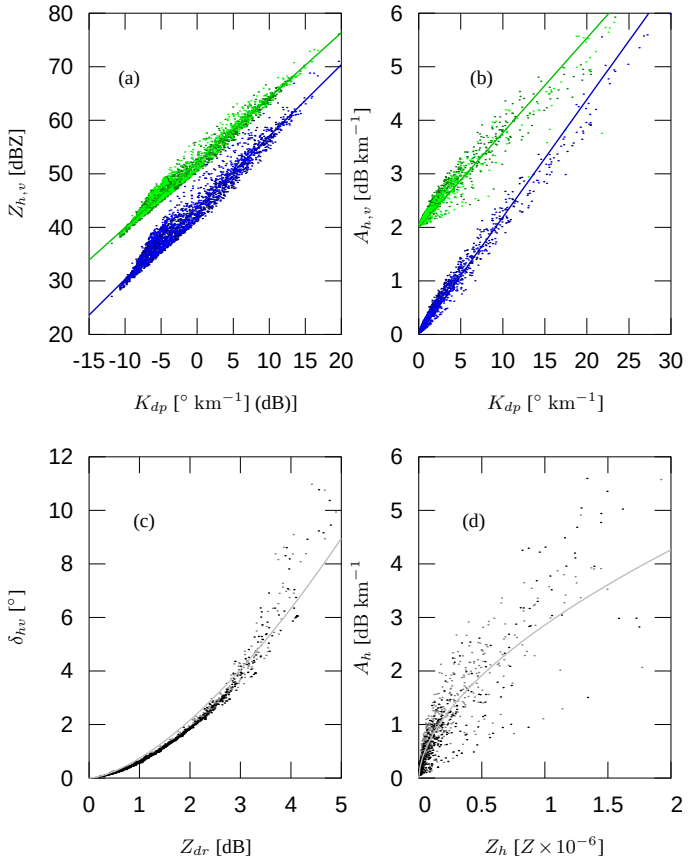

Fig. 5. T-matrix modeled relations between polarimetric variables: **(a)** horizontally (Z_h; blue) and vertically (Z_v; green) polarized reflectivity versus K_{dp}. Z_v is plotted with an artificial offset of 10 dB for clarity. **(b)** Horizontally (A_h; blue) and vertically (A_v; green) polarized specific attenuation versus K_{dp}. A_v is plotted with an artificial offset of 2 dB for clarity. **(c)** Backscatter differential phase shift δ_{hv} versus the differential reflectivity Z_{dr}. **(d)** A_h versus Z_h.

AMTD
5, 1717–1761, 2012

Firts results from the CHUVA campaign

M. Schneebeli et al.

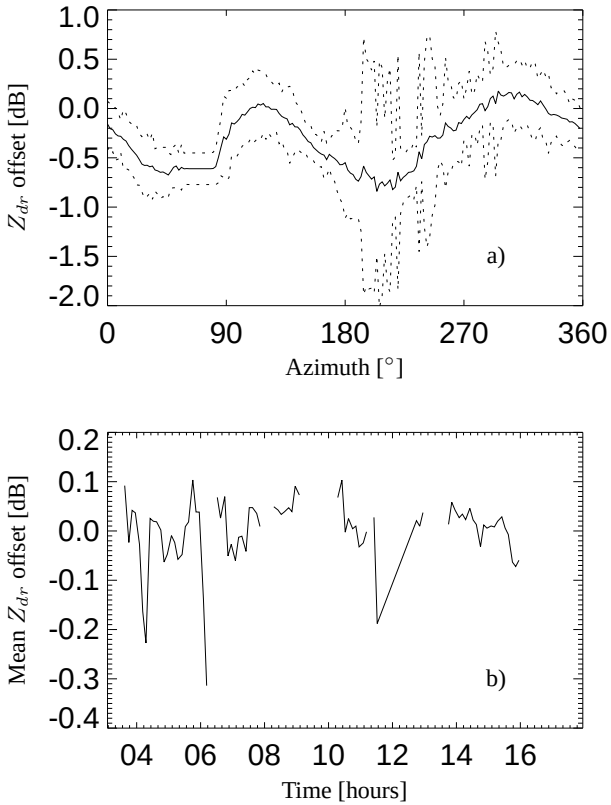

Fig. 6. **(a)** Z_{dr} offset as a function of the azimuth angle measured over a period of 12 h on 12 April 2011. The black line shows the mean offset over this period and the dotted lines indicate the standard deviation. **(b)** Time series of the mean Z_{dr} offset.

AMTD
5, 1717–1761, 2012

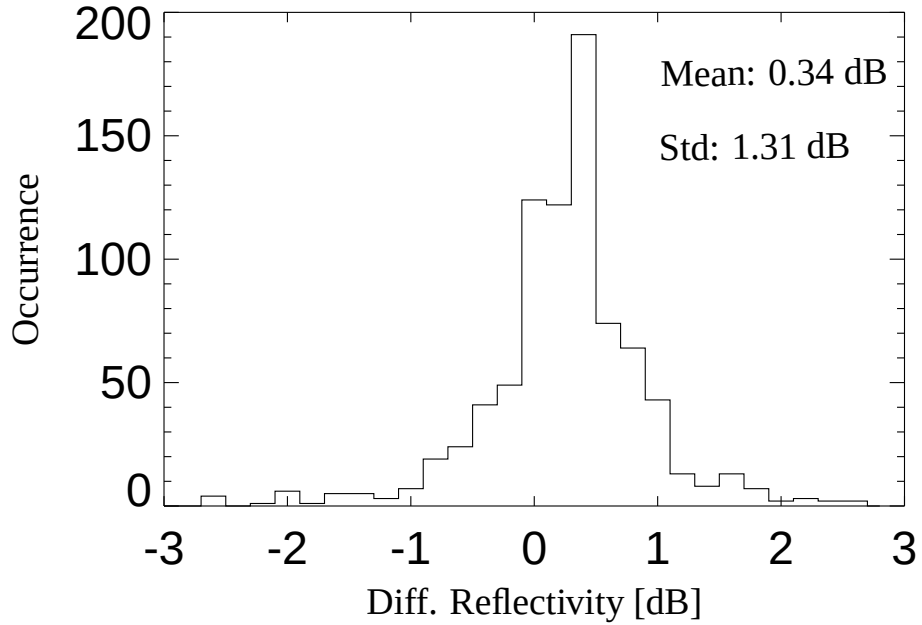

Fig. 7. Histogram of Z_{dr} values found in conditions of low reflectivity and low attenuation.

AMTD
5, 1717–1761, 2012

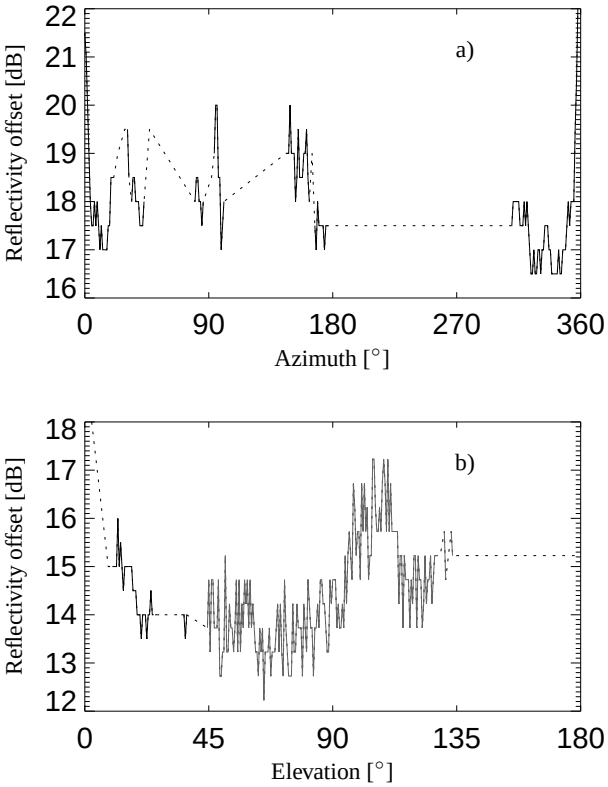

Fig. 8. **(a)** Reflectivity offset as a function of the azimuth angle, measured on 12 April 2011, 05:20 UTC. The black lines indicate values that are determined with the EKF algorithm, while dashed lines show interpolated values. **(b)** Same as in **(a)** but as a function of the elevation angle. In addition to the plot in panel **(a)**, the grey line shows values that are determined from the scaling of the reflectivity value at the first range gate as described in the foregoing section.

AMTD
5, 1717–1761, 2012

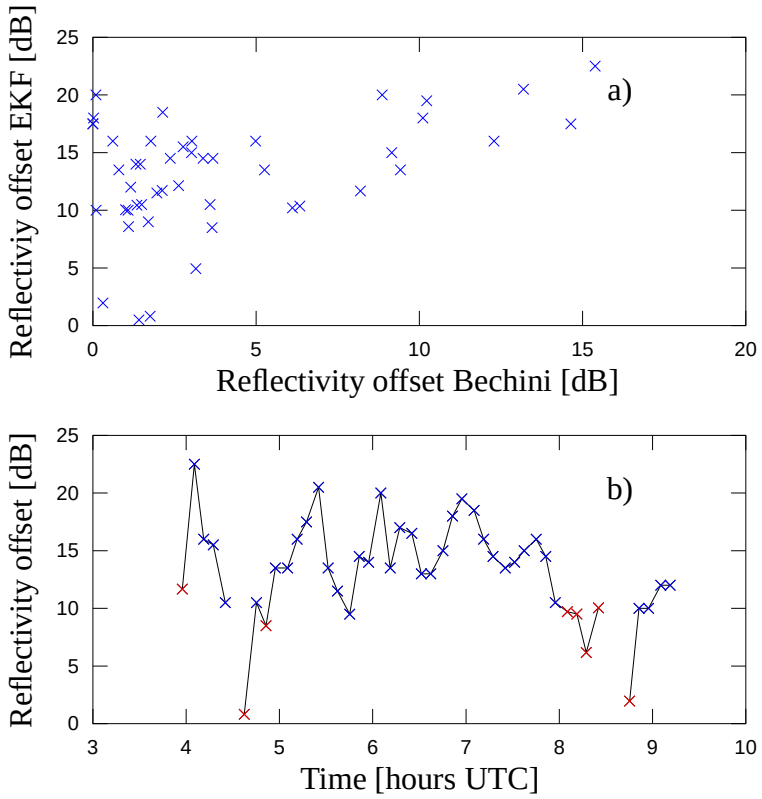

Fig. 9. **(a)** Scatter plot of the reflectivity offsets determined with the method of Bechini et al. (2010) and the EKF algorithm. **(b)** Time series of reflectivity offsets determined with the EKF method (blue crosses) and with the K_{dp} method (red crosses).

AMTD
5, 1717–1761, 2012

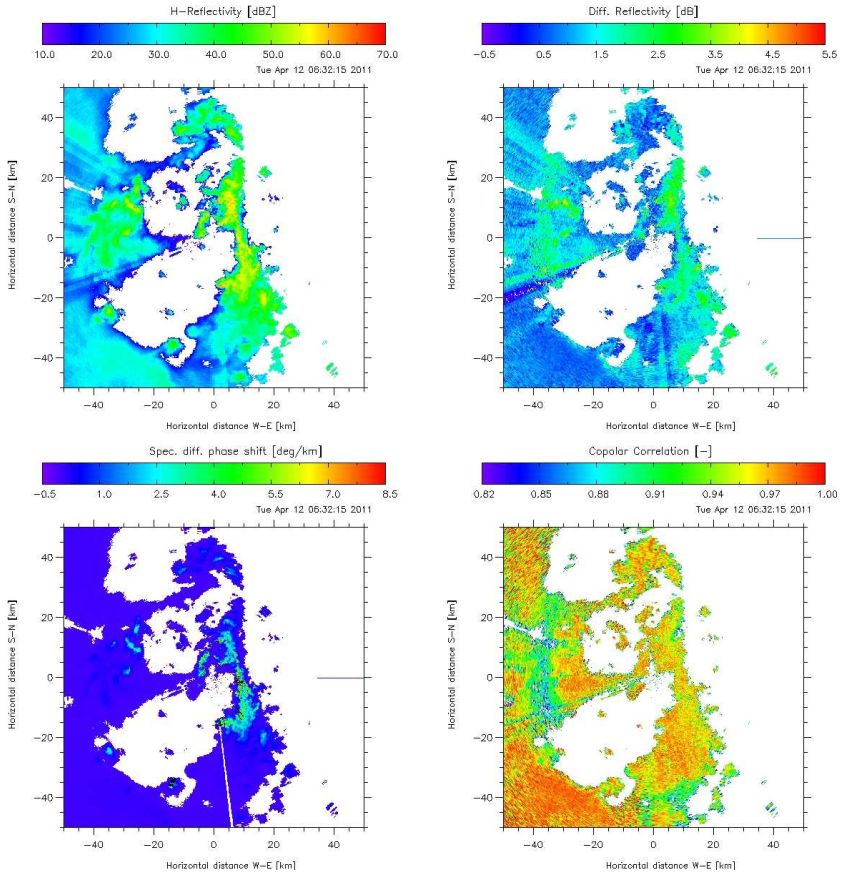

Fig. 10. Example of the polarimetric observables from one PPI scan performed on 12 April 2011 at an elevation of 5.3°. Note that the streak around 250° is associated to an antenna of a radio telescope that was located in close distance to the radar.

AMTD
5, 1717–1761, 2012

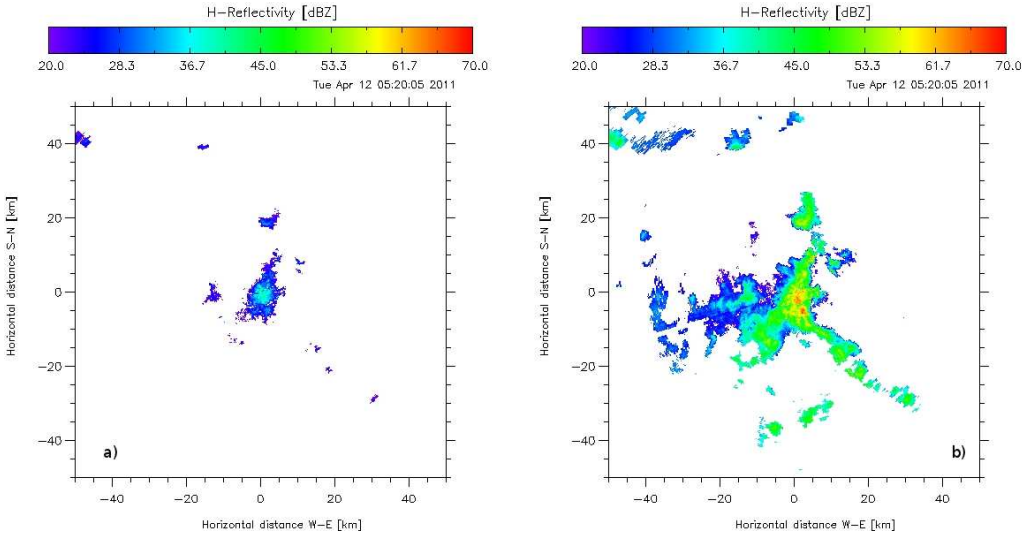

Fig. 11. (a) PPI scan showing uncorrected reflectivity. **(b)** The same scan that is shown in **(a)** but after radome and rain attenuation correction with the EKF algorithm.

AMTD
5, 1717–1761, 2012

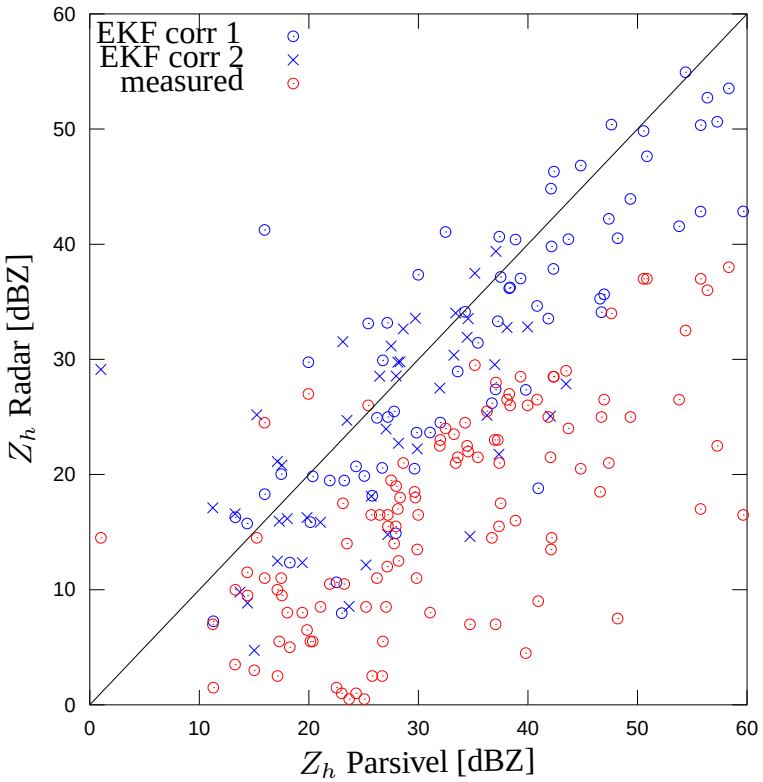

Fig. 12. Scatter plot of the reflectivity Z_h [dB] inferred from DSD measurements of a Parsivel disdrometer versus radar measurements performed at the range gate and direction corresponding to the location of the disdrometer. The distance between the disdrometer and the radar is 20 km. Red circles show raw (uncorrected) radar measurements, blue circles and crosses show data treated with the EKF algorithm, where the crosses indicate that the offset is determined with the K_{dp} method instead of the EKF method.

AMTD
5, 1717–1761, 2012

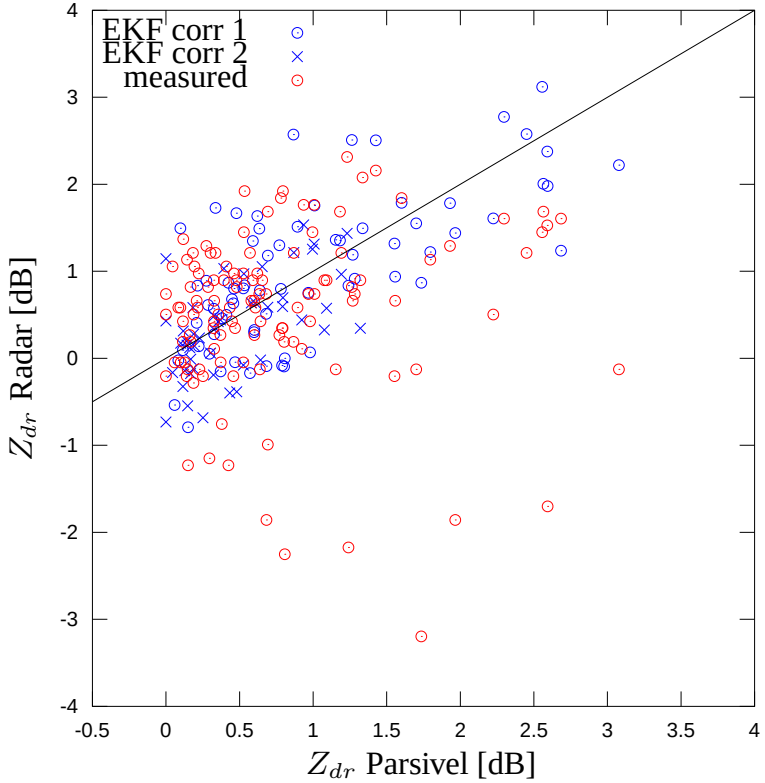

Fig. 13. Same as in Fig. 12 but for Z_{dr}.

AMTD
5, 1717–1761, 2012

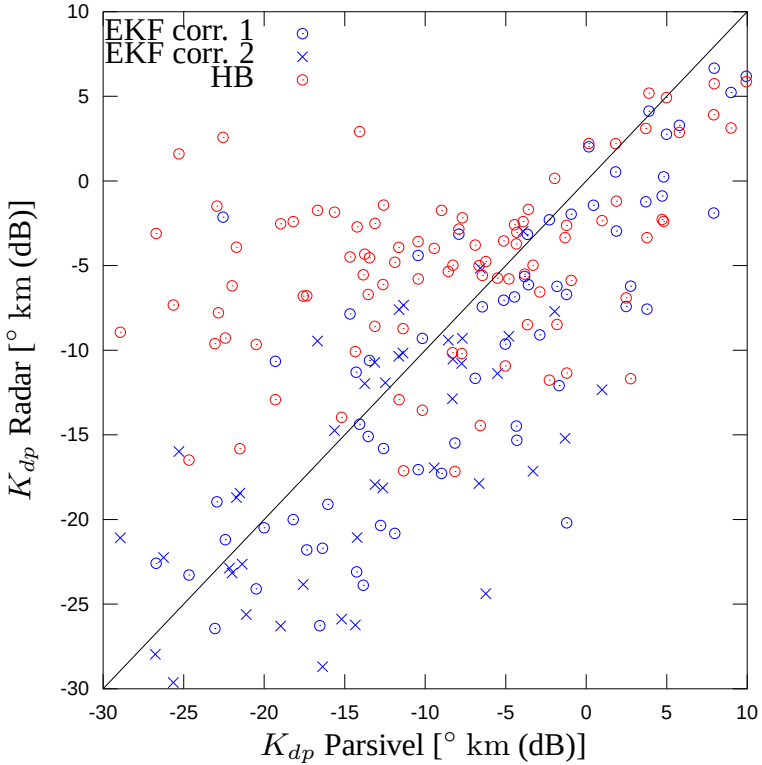

Fig. 14. Same as in Fig. 12 but for K_{dp}. Note that K_{dp} is not directly measured with a radar, hence the EKF data is compared to K_{dp} data inferred with the algorithm of Hubbert and Bringi (1995).

AMTD
5, 1717–1761, 2012